Ultra-High-Energy Particle Production in Binary Mergers Endowed with Magnetic Fields

Carlos H. Coimbra-Araújo[1,2],* Rita C. Anjos[1,2,3,4,5,6], Jonas P. Pereira[5,6,7], and Jaziel G. Coelho[8,9]
[1]*Departamento de Engenharias e Exatas, Universidade Federal do Paraná (UFPR), Rua Pioneiro, Palotina, 85950-000, PR, Brazil.*
[2]*Programa de Pós-Graduação em Física Aplicada, Universidade Federal da Integração Latino-Americana, Av. Tarquínio Joslin dos Santos, 1000, Foz do Iguaçu, 85867-670, PR, Brazil.*
[3] *Centro de Artes, Humanidades e Tecnologia, Universidade Federal de São Carlos (UFSCar), R. Dr. Eduardo Nielsen, 420, Jardim Congonha, São José do Rio Preto, 15030-070, SP, Brazil*
[4]*Programa de pós-graduação em Física & Departamento de Física, Universidade Estadual de Londrina (UEL), Rodovia Celso Garcia Cid Km 380, Londrina, 86057-970, PR, Brazil.*
[5]*Programa de Pós-Graduação em Física e Astronomia, Universidade Tecnológica Federal do Paraná (UTFPR), Av. Sete de Setembro, 3165, Curitiba, 80230-901, PR, Brazil.*
[6] *Programa de Pós-Graduação em Astrofísica, Cosmologia e Gravitação (PPGCosmo), Federal University of Espírito Santo, Vitória-ES, 29075-910, Brazil*
[7]*Institute of Physics & International Center of Physics, University of Brasilia, 70297-400, Brasilia, Federal District, Brazil.*
[8] *Nicolaus Copernicus Astronomical Center, Polish Academy of Sciences, Bartycka 18, 00-716, Warsaw, Poland*
[9]*Departamento de Física, Universidade Federal do Espírito Santo, Núcleo de Astrofísica e Cosmologia (Cosmo-Ufes), Av. Fernando Ferrari, 514, Vitória, 29075-910, ES, Brazil. and*
[10]*Divisão de Astrofísica, Instituto Nacional de Pesquisas Espaciais, São José dos Campos, 12227-010, SP, Brazil.*
(Dated: July 24, 2026)

We study the production of ultra-high-energy particles via the Bañados–Silk–West (BSW) mechanism in the pre-merger phase of binary systems detected by LIGO-Virgo-KAGRA. By solving the geodesic equations for charged particles in magnetized Kerr spacetime with fields of $B \sim 10^{12}$–10^{14} G, we demonstrate that collisions near the horizon can achieve center-of-mass energies $E_{\rm cm} \sim 10^{18}$– 10^{20} eV, placing them firmly in the ultra-high-energy cosmic-ray (UHECR) range. We systematically explore the parameter space of merger remnants, varying black hole mass ($M \sim 20$–$150\,M_\odot$, characteristic of the binary black hole population), dimensionless spin ($\chi_f \sim 0.7$–0.9), magnetic field strength, and particle angular momenta. Our analysis reveals three distinct acceleration regimes: a gravity-dominated regime ($B < 10^{12}$ G) with negligible magnetic enhancement; a transition regime (10^{12} G $\lesssim B \lesssim 10^{13}$ G) where gravitational and magnetic effects compete; and a magnetic-dominated regime ($B > 10^{13}$ G) where fields amplify collision energies by nearly an order of magnitude. For the 34 gravitational-wave events with high remnant spins ($\chi_f > 0.7$), we compute the maximum achievable energies, finding that systems with $\chi_f \gtrsim 0.85$ and $M \gtrsim 100\,M_\odot$ can reach $E_{\rm max} \sim 10^{20}$ eV. Our results establish magnetized binary mergers, particularly black hole–neutron star systems and postmerger black hole remnants formed in binary neutron star coalescences, as promising sources of UHECRs and provide quantitative predictions linking gravitational-wave observables to particle acceleration efficiency.

arXiv:2607.21385v1 [astro-ph.HE] 23 Jul 2026

I. INTRODUCTION

As cosmic rays traverse the universe, they span an extraordinary range of energies. The most energetic of these, known as ultra-high-energy cosmic rays (UHECRs), are detected by ground-based facilities such as the Pierre Auger Observatory [1] and the Telescope Array [2]. Their potential astrophysical origins encompass a diverse set of extreme environments, including active galactic nucleus jets, gamma-ray bursts from massive stellar collapse, jets and shocks from tidal disruption events, as well as acceleration in giant radio lobes and large-scale extragalactic structure formation shocks. Comprehensive reviews of these acceleration scenarios can be found in Refs. [3, 4].

A key motivation for studying UHECRs is that their energies exceed the Greisen-Zatsepin-Kuzmin (GZK) threshold of $E > 10^{18}$ eV [5, 6], above which interactions with the cosmic microwave background are expected to suppress the flux of extragalactic cosmic rays. Recent observations indicate that the composition of extragalactic cosmic rays evolves with energy, with measurements suggesting a transition from lighter to heavier nuclei as energies increase from a few EeV toward 10^{20} eV [7, 8]. These observations naturally lead to fundamental questions concerning both the astrophysical origin and the acceleration mechanisms capable of producing such extreme particle energies.

* carlos.coimbra@ufpr.br

The most widely discussed acceleration mechanisms include variants of Fermi's original proposal, wherein charged particles gain energy through repeated interactions with magnetized plasma structures. However, the classical Fermi mechanism is too slow and inefficient to directly produce UHECRs. This has motivated alternative proposals, most prominently diffusive shock acceleration at astrophysical shock fronts [4, 9], where particles gain energy through repeated crossings of shock discontinuities in the presence of magnetic turbulence [10, 11]. Modern numerical simulations using particle-in-cell codes [12, 13] such as `Sapphire++` [14, 15] have provided detailed insights into the microphysics of collisionless shocks and particle injection mechanisms. Nevertheless, theoretical constraints on particle propagation [16] and observational measurements of the cosmic-ray spectrum and composition suggest significant challenges for shock acceleration models at the highest energies. Even state-of-the-art treatments incorporating oblique shock geometries in supernova remnants embedded in massive star clusters, tuned to reproduce the LHAASO knee spectrum and composition, remain confined to multi-PeV energies [17], well below the EeV–ZeV regime relevant for UHECRs. Consequently, alternative acceleration processes associated with particle dynamics in the extreme gravitational and electromagnetic environments near compact astrophysical objects have attracted increasing attention [18–20].

One particularly compelling mechanism involves particle collisions near rotating black holes (BHs), where ultra-high center-of-mass energies can be achieved through the Bañados-Silk-West (BSW) effect [21]. This mechanism exploits the unique properties of Kerr spacetime, wherein particles traversing the ergosphere can acquire negative energy as measured by observers at infinity [22], and collisions between particles with critical angular momenta near the event horizon can produce arbitrarily high center-of-mass energies for near-extremal rotation parameters approaching $a = M$. Such scenarios have been investigated for various black hole configurations, including static [21], rotating [21, 23], charged [24], and weakly magnetized [25, 26] systems, as well as for strongly magnetized black holes with arbitrary spin parameters [19, 20]. However, common criticisms of the standard BSW mechanism concern its efficiency and physical plausibility [23, 27–29]. While the center-of-mass energy of the collision can, in principle, become arbitrarily large, this does not in general translate into equally large energies for particles that can actually escape to, and be detected at, infinity. In fact, several studies have established upper bounds on the received energy [27–30], in part because collisions that take place extremely deep in the gravitational potential well suffer a large gravitational redshift for the outgoing debris. Notwithstanding, these bounds can be significant in some configurations [30–32]. Therefore, as emphasized in Berti *et al.* [32], scenarios that go beyond the standard BSW mechanism—most notably those including magnetic fields—are far more relevant from both a physical and an observational standpoint [33]. In this work, we focus precisely on such magnetized setups.

An additional challenge for conventional UHECR source models is that even if individual sources generate a narrowly peaked rigidity spectrum, the luminosity functions observed for active galactic nuclei, long gamma-ray bursts, tidal disruption events, and other candidate systems are too broad to be compatible with the narrow rigidity distribution inferred for UHECRs [34]. This incompatibility has motivated suggestions of alternative source populations, including binary neutron star (BNSs) mergers [35, 36], black hole-neutron star (BH-NS) mergers, and binary black hole coalescences (BBHs or BH-BH binaries), which may produce more homogeneous acceleration conditions.

In previous work [37], we established magnetized pre-merger binaries, especially BH-NS ones (but also BBHs binaries with at least one of them charged and with an accretion disk), as plausible UHECR sources via a magnetically enhanced BSW mechanism, demonstrating that astrophysical magnetic fields ($B \gtrsim 10^{10}$ G) enable ultra-high-energy collisions for generic, high-spin remnants. We showed that this result is largely independent of the black hole spin parameter, a/M, and of the black hole mass, occurring across a broad range of both quantities. In our scenario, UHECRs would be produced prior to merger—which could yield a cleaner observational signature—and the number of such particles could reach the millions. The same mechanism may also operate after the merger if the neutron star is tidally disrupted, since the essential ingredients—magnetic fields, a black hole horizon, and particles—remain present. This paper provides the detailed quantitative foundation for that result and derives explicit scaling relations for the maximum particle energy $E_{\rm max}$. We systematically solve the geodesic equations for charged particles in magnetized Kerr spacetime, explore the full parameter space relevant to binary merger remnants detected by LIGO-Virgo-KAGRA, and compute center-of-mass collision energies for all high-spin gravitational wave events. Our analysis identifies the dominant physical effects controlling particle acceleration efficiency and establishes quantitative predictions linking gravitational-wave observables to UHECR production.

This paper is organized as follows. In Section II, we present the theoretical framework for particle motion in magnetized Kerr spacetime, deriving the equations of motion, conserved quantities, and center-of-mass energy expressions. We also introduce the scaling relations for maximum achievable energies and describe our computational implementation. Section III presents our main results, including the dependence of collision energies on magnetic field strength, black hole mass and spin, radial location, and particle angular momenta. We apply our framework to the catalog of gravitational wave events and discuss the astrophysical implications. Finally, Section IV summarizes our conclusions and dis-

cusses prospects for multi-messenger observations with third-generation gravitational wave detectors and next-generation cosmic ray observatories.

II. UHE PARTICLE PRODUCTION IN BINARY BLACK HOLE MERGERS

The production of UHECRs through particle collisions near rotating black holes represents a compelling theoretical framework for understanding the origin of the most energetic particles observed in nature. This mechanism exploits the unique properties of spacetime near rapidly spinning black holes, where the combination of strong gravitational fields and electromagnetic interactions can produce extraordinary center-of-mass collision energies. The physical basis for this acceleration mechanism lies in the peculiar structure of rotating black hole spacetimes, first elucidated by Penrose [22], wherein particles traversing the ergosphere [1] can acquire negative energy as measured by observers at infinity. When such negative-energy particles are captured by the horizon, mass and angular momentum can be extracted from the black hole itself, a process that has profound implications for particle energetics in the vicinity of the horizon.

The collisional variant of this energy extraction mechanism, known as the BSW effect [21], demonstrates that particle collisions occurring extremely close to the horizon of a near-extremal rotating black hole ($a \to M$, where a is the black hole angular momentum parameter) can yield arbitrarily high center-of-mass energies. This remarkable result follows from the structure of null geodesics and particle trajectories in Kerr spacetime, where certain critical values of particle angular momentum lead to resonant enhancement of collision energies. While the original BSW analysis considered vacuum geodesics, realistic astrophysical contexts, particularly those associated with black holes at the centers of galaxies and after the merger of two neutron stars (NSs) are expected to harbor substantial magnetic fields threading the black hole magnetosphere. These fields, generated either by residual accretion flows, magnetized stellar winds from companion objects, or reconnection processes in the merger environment, fundamentally modify particle trajectories and can significantly enhance the efficiency of the acceleration mechanism. In the pre-merger context, strong magnetic fields may also be present close to the event horizon and can enhance the efficiency of the BSW mechanism. The most natural setting is a BH–NS binary at separations of only a few neutron-star radii. In this case, as discussed in [37], magnetic fields as large as 10^{12}–10^{14}G may arise in small regions of the black-hole ergosphere. Another possible route to such strong fields would involve charged black holes: we have shown that charge-to-mass ratios as small as 10^{-5} would already suffice. Whether astrophysical black holes can sustain such a charge, however, remains an open question. By contrast, BH–NS binaries are expected, essentially inevitably, to lead to very large magnetic fields in the near-horizon region in the instants immediately preceding merger.

The mathematical description of particle motion in such magnetized rotating black hole spacetimes requires the Kerr metric, which generalizes the spherically symmetric Schwarzschild solution to incorporate the effects of black hole spin. The presence of rotation breaks spherical symmetry, yielding instead an axially symmetric geometry characterized by frame-dragging effects that become increasingly pronounced as the spin parameter approaches the extremal limit $a \to M$. In this geometry, the energy and angular momentum about the rotation axis are modified by electromagnetic interactions, leading to a rich phenomenology of acceleration and energy extraction processes.

A. Kerr Spacetime and conserved quantities

A rotating black hole is described by the Kerr metric, which exhibits axial symmetry rather than the spherical symmetry of non-rotating solutions. In Boyer-Lindquist coordinates, the spacetime geometry is characterized by the line element

$$ds^2 = g_{tt}dt^2 + 2g_{t\phi}dtd\phi + g_{rr}dr^2 + g_{\theta\theta}d\theta^2 + g_{\phi\phi}d\phi^2, \quad (1)$$

where the metric components are

$$g_{tt} = -\left(1 - \frac{2Mr}{\Sigma}\right), \quad (2)$$

$$g_{t\phi} = -\frac{2aMr\sin^2\theta}{\Sigma}, \quad (3)$$

$$g_{rr} = \frac{\Sigma}{\Delta}, \quad (4)$$

$$g_{\theta\theta} = \Sigma, \quad (5)$$

$$g_{\phi\phi} = \frac{(r^2+a^2)^2 - a^2\Delta\sin^2\theta}{\Sigma}\sin^2\theta, \quad (6)$$

with $\Sigma = r^2 + a^2\cos^2\theta$ and $\Delta = r^2 + a^2 - 2Mr$. Here, M represents the black hole mass and a is the angular momentum parameter. The event horizon is located at $r_H = M + \sqrt{M^2 - a^2}$, while the ergosphere extends from r_H to $r_E(\theta) = M + \sqrt{M^2 - a^2\cos^2\theta}$.

[1] region between the event horizon and the static limit

The presence of two Killing vectors associated with time translation symmetry

$$\xi_{(t)} = \xi^{\mu}_{(t)}\partial_{\mu} = \frac{\partial}{\partial t}, \tag{7}$$

and axial rotation symmetry

$$\xi_{(\phi)} = \xi^{\mu}_{(\phi)}\partial_{\mu} = \frac{\partial}{\partial \phi}, \tag{8}$$

leads to two conserved quantities for particle motion. For a test particle with four-momentum p_μ following a geodesic in vacuum, these conserved quantities represent the particle's energy and angular momentum as measured by an observer at spatial infinity.

B. Electromagnetic interactions and modified geodesics

When charged particles move through regions threaded by magnetic fields, their trajectories deviate from pure geodesics according to the equation of motion

$$\ddot{x}^{\mu} + \Gamma^{\mu}_{\alpha\beta}\dot{x}^{\alpha}\dot{x}^{\beta} = \frac{q}{m_0}F^{\mu}_{\nu}\dot{x}^{\nu}, \tag{9}$$

where $F_{\mu\nu} = A_{\nu,\mu} - A_{\mu,\nu}$ is the electromagnetic field tensor, A_μ is the four-potential, q is the particle charge, and m_0 is the rest mass. The overdot denotes differentiation with respect to proper time τ, and $\Gamma^{\mu}_{\alpha\beta}$ are the Christoffel symbols derived from the metric. For an approximately uniform magnetic field B threading the black hole magnetosphere, we adopt the Lorentz gauge condition, which simplifies the electromagnetic four-potential to a single non-vanishing component: $A_\phi = Bg_{\phi\phi}/2$. This choice assumes a large-scale, ordered magnetic field—as expected in a rotating black hole magnetosphere or in the plasma around merging compact objects—and reflects that the particle collision region is confined to a small neighborhood of the black hole. Indeed, the assumption of a uniform magnetic field is intended strictly as a local approximation. Our analysis is focused on the dynamics in the immediate vicinity of the collision region, near the ISCO, where the interaction takes place. In this context, the uniform magnetic field should be interpreted as a local approximation, valid within a sufficiently small spacetime neighborhood of the collision event. This is analogous to employing a locally inertial frame in curved spacetime: while the global structure is nontrivial, it can be approximated as uniform at leading order in a small region.

The particle's canonical four-momentum $p_\mu = m_0 u_\mu + qA_\mu$ then yields modified expressions for the conserved quantities:

$$\mathcal{E} = -g_{t\mu}(m_0 u^{\mu} + qA^{\mu}), \tag{10}$$

and

$$\ell = g_{\phi\mu}(m_0 u^{\mu} + qA^{\mu}), \tag{11}$$

where $u^\mu = \dot{x}^\mu$ is the four-velocity. For convenience, we work with the dimensionless angular momentum $\ell \equiv L/(Mm_0)$, where L is the physical angular momentum. These modified conservation laws fundamentally alter the allowed particle trajectories compared to the vacuum case. The presence of magnetic fields shifts the location of stable circular orbits of particles and modifies the effective potential governing radial motion, thereby changing the conditions under which particles can escape to infinity or plunge into the black hole.

C. Four-Velocity components in the equatorial plane

For particles confined to the equatorial plane ($\theta = \pi/2$, $\dot{\theta} = 0$), which we adopt for simplicity, the four-velocity components can be determined from the conservation laws and the normalization condition $g_{\mu\nu}u^\mu u^\nu = -1$. Introducing the normalized magnetic field parameter $\mathcal{B} \equiv qB/(2m_0)$, the angular velocity component is given by:

$$\dot{\phi} = \frac{g_{tt}L/m_0 + g_{\phi t}\mathcal{E}/m_0 - g_{tt}g_{\phi\phi}\mathcal{B}}{g_{tt}g_{\phi\phi} - g_{t\phi}^2}. \tag{12}$$

The temporal component of the four-velocity follows from the energy conservation law:

$$\dot{t} = \frac{-\mathcal{E}/m_0 - g_{t\phi}\dot{\phi}}{g_{tt}}, \tag{13}$$

while the radial component is determined by the normalization condition:

$$\dot{r} = \sqrt{\frac{-1 - g_{tt}\dot{t}^2 - 2g_{t\phi}\dot{t}\dot{\phi} - g_{\phi\phi}\dot{\phi}^2}{g_{rr}}}. \tag{14}$$

These equations determine the complete trajectory of a charged particle in the combined gravitational and electromagnetic field. The radial component $\dot{r}$ must be real and positive for physically meaningful solutions, which constrains the allowed values of $\mathcal{E}$ and ℓ for particles that can escape to infinity.

D. Center-of-Mass energy and the BSW mechanism

The center-of-mass energy for a collision between two particles, each of rest mass m_0, is determined by the relativistic invariant:

$$E_{c.m.} = \sqrt{2} m_0 \sqrt{1 - g_{\mu\nu} u^{\mu}_{(1)} u^{\nu}_{(2)}}, \tag{15}$$

where $u^{\mu}_{(1)}$ and $u^{\nu}_{(2)}$ are the four-velocities of the colliding particles, normalized such that $g_{\mu\nu} u^{\mu} u^{\nu} = -1$ for each particle. Expanding the metric contraction explicitly for equatorial orbits yields:

$$E_{c.m.} = \sqrt{2} m_0 \Big[1 + g_{tt} \dot{t}_{(1)} \dot{t}_{(2)} + g_{t\phi} (\dot{t}_{(1)} \dot{\phi}_{(2)} + \dot{t}_{(2)} \dot{\phi}_{(1)}) + g_{rr} \dot{r}_{(1)} \dot{r}_{(2)} + g_{\phi\phi} \dot{\phi}_{(1)} \dot{\phi}_{(2)} \Big]^{1/2}. \tag{16}$$

The remarkable feature of this framework, first identified by Bañados, Silk, and West [21], is that center-of-mass energies can become arbitrarily large for specific particle configurations near extremal black holes ($a \to M$). This enhancement occurs when one or both colliding particles possess critical values of angular momentum. The physically accessible range for the dimensionless angular momentum parameter is constrained to

$$-2(1 + \sqrt{1 + a/M}) < \ell < 2(1 + \sqrt{1 - a/M}) \tag{17}$$

to ensure particles can escape to infinity after the collision [30]. The dominant factors controlling the achievable collision energies are: (i) the black hole spin parameter a/M, which determines the location of the innermost stable circular orbit and the structure of the ergosphere; (ii) the strength and configuration of magnetic fields, which modify particle trajectories and can facilitate particle escape; and (iii) the angular momentum values ℓ_1 and ℓ_2 of the colliding particles, with critical values leading to resonant energy enhancement.

E. Scaling relations and Maximum achievable energies

The maximum center-of-mass energy achievable in the magnetized Kerr geometry depends on the interplay between black hole mass, spin, magnetic field strength, and the conserved quantities of the colliding particles. Through systematic exploration of the parameter space defined by Eq. (17), we can identify configurations that maximize $E_{\rm c.m.}$ for given values of M, $\chi_f \equiv a/M$, and B. The center-of-mass energy computed from Eq. (16) exhibits a characteristic scaling with black hole mass that can be expressed as:

$$E_{\rm max} = m_0 c^2 \left(\frac{M}{M_\odot} \right) \mathcal{F}(\chi_f, \mathcal{B}, \ell_1, \ell_2), \tag{18}$$

where $\mathcal{F}(\chi_f, \mathcal{B}, \ell_1, \ell_2) = \left(\frac{\chi_f}{0.9}\right) \sqrt{1 - g_{\mu\nu} u^{\mu}_{(1)} u^{\nu}_{(2)}}$ is the dimensionless amplification function that encapsulates the complex dependence on the spin parameter χ_f, the normalized magnetic field strength $\mathcal{B} \equiv qB/(2m_0 c)$, and the angular momenta ℓ_1 and ℓ_2 of the colliding particles. This function cannot be expressed in closed analytical form but must be determined through numerical solution of the coupled equations (12)–(14) and (16) at each point in parameter space. The linear scaling with black hole mass reflects the geometric nature of the gravitational acceleration mechanism, where the relevant energy scale is set by $m_0 c^2 (M/M_\odot)$ in natural units.

The amplification function $\mathcal{F}$ exhibits strong sensitivity to the black hole spin parameter, with values increasing dramatically as $\chi_f \to 1$. This enhancement reflects both the intensified frame-dragging effects near extremal black holes and the approach to critical angular momentum values that trigger divergent behavior in the BSW mechanism. We work with magnetic fields of neutron stars, magnetars and BNS post-merger events that could reach up to $B \sim 10^{12} - 10^{14}$ G (see Sec. IIG and references therein). In this case, the normalized field parameter takes values $\mathcal{B} \sim 10^{-6} - 10^{-4}$ for protons. At these field strengths, the electromagnetic modifications to the geodesic structure become significant, shifting the effective locations of stable orbits and altering the energy extraction efficiency.

For sub-extremal black holes with spins $\chi_f \sim 0.7 - 0.9$ as commonly observed in gravitational wave merger events, and adopting fiducial parameters $M \sim 100\, M_\odot$ and $B \sim 10^{14}$ G, our numerical calculations yield amplification factors in the range $\mathcal{F} \sim 10^{11} - 10^{13}$. These values correspond to maximum center-of-mass energies:

$$E_{\rm max} \sim 10^{17} - 10^{20} \left(\frac{M}{100\, M_\odot} \right) \left(\frac{\chi_f}{0.9} \right) \text{ eV}, \tag{19}$$

placing the collision energies squarely in the ultra-high-energy cosmic ray regime. The upper end of this range, approaching 10^{20} eV, is achieved for systems with both high spin ($\chi_f \gtrsim 0.85$) and optimal choices of particle angular momenta that maximize the resonant enhancement. The amplification function $\mathcal{F}$ depends most sensitively on the angular momentum ℓ_1 of the first particle, with peak values occurring when ℓ_1 approaches the critical value $\ell_{\rm crit} \approx 2$ for near-extremal configurations. The second particle's angular momentum ℓ_2 must be chosen from the opposite end of the allowed range to ensure constructive interference in the energy extraction process.

The magnetic field dependence encoded in $\mathcal{F}$ exhibits a more gradual variation compared to the spin dependence. For field strengths varying from $B = 10^{12}$ G to $B = 10^{14}$ G while holding other parameters fixed, the amplification factor increases approximately as $\mathcal{F} \propto B^{0.3-0.5}$, indicating a sub-linear enhancement with magnetic field strength. This scaling reflects the competing effects of electromagnetic acceleration, which increases with B, and magnetic confinement, which can suppress particle

escape at very high field strengths. The optimal field strength for maximum energy extraction depends on the specific values of χ_f and the collision geometry, but typically falls in the range $B \sim 10^{13} - 10^{14}$ G for stellar-mass systems.

F. Computational Implementation

To determine the maximum center-of-mass energy achievable for a given black hole configuration, we solve the coupled system of equations defined by Eqs. (12)–(14) and (16). For specified values of black hole mass M, spin parameter χ_f, and magnetic field strength $B = 10^{14}$ G, we first calculate the metric components at a chosen radius $r = r_H + \varepsilon$, where ε is a small distance from the event horizon. We typically adopt $\varepsilon = 10^{-10} M$ to ensure proximity to the horizon while maintaining numerical stability. For each pair of colliding particles labeled $i = 1, 2$, we fix the energies at $\mathcal{E}_i/m_0 = 1$ and systematically vary the angular momenta ℓ_i within the allowed range given by Eq. (17). For each choice of parameters, we compute the four-velocity components using Eqs. (12)–(14) and verify that the normalization condition $g_{\mu\nu} u^\mu u^\nu = -1$ is satisfied to within numerical precision. We then calculate the center-of-mass energy using Eq. (16) and record the maximum value obtained across the entire (ℓ_1, ℓ_2) parameter space. This procedure requires careful numerical treatment near critical values of angular momentum where the energy exhibits rapid variation, as well as verification that the resulting particle trajectories correspond to physically realizable configurations that allow escape to infinity.

G. Application to Binary Black Hole Mergers

For binary black hole systems detected through gravitational waves, the final merged black hole is characterized by a mass M and dimensionless spin parameter $\chi_f \equiv a/M$. This mass range, $M \sim 20$–$150\, M_\odot$, applies specifically to the BBH population. BH-NS and BNS remnants are treated separately below and occupy much lower remnant masses, dominated by the neutron star component. Recent observations from LIGO-Virgo-KAGRA reveal that many merger remnants possess high spins, with $\chi_f > 0.7$ being common [38–40]. Such rapidly rotating black holes provide favorable conditions for efficient particle acceleration through the BSW mechanism.

The magnetic field strength near merging black holes depends on the astrophysical environment and remains uncertain, but theoretical considerations suggest plausible values. For BH–BH binaries in which one of the components carries a charge-to-mass ratio of 10^{-4}–10^{-3},[2] field strengths in the range $B \sim 10^{12}$–10^{14} G are plausible (see the Supplemental Material of [37], where we showed that charge-to-mass ratios of 10^{-5} lead to field strengths of $B \sim 10^{11}$–10^{12} G at $r = 2r_h$). To have upper limits, we adopt $B = 10^{14}$ G as our fiducial value. It is motivated by extreme but astrophysically plausible scenarios. Post-merger amplification mechanisms in BBH remnants can generate intense fields in the surrounding plasma [42–48]. The inclusion of magnetic fields up to 10^{14} G therefore allows us to explore the maximum acceleration capabilities of compact-object mergers without altering the conclusions obtained for more moderate field strengths.

For the population of binary black hole mergers detected to date, the final masses span the range $M \sim 20$–$150\, M_\odot$ with typical values around 50–$70\, M_\odot$, while the measured spins cluster in the range $\chi_f \sim 0.7$–0.9 with occasional systems reaching $\chi_f > 0.9$. Applying our computational framework to these observed parameter combinations, we find maximum center-of-mass energies spanning $E_{\rm max} \sim 10^{18}$–10^{20} eV. These values place the BSW mechanism operating in binary black hole mergers squarely in the regime of ultra-high-energy cosmic rays as observed by the Pierre Auger Observatory and other large-scale detectors. The specific energy achieved for each merger event depends sensitively on the final spin through both the direct scaling in Eq. (18) and the implicit dependence through the function f, with higher-spin systems producing systematically higher maximum energies. This correlation between gravitational wave observables, specifically the inferred remnant spin, and the predicted UHECR production provides a testable prediction of this acceleration scenario.

H. BH-NS and BNS channels

We now comment separately on the BH-NS and BNS channels, whose remnant masses and field-sustaining mechanisms differ substantially from those of the BBH population discussed above and are not represented in Table I.

For BH-NS binaries with separations on the order of a few neutron-star radii, or for post-merger BHs formed in binary neutron-star mergers, field strengths in the range $B \sim 10^{12}$–10^{14} G have also been suggested. In BH-NS mergers, magnetar companions may possess surface magnetic fields of 10^{14}–10^{15} G, and post-merger amplification mechanisms can generate similarly intense fields in the surrounding plasma [42–48]. We discuss the physical viability of the disk-anchored field scenario, and its restric-

[2] We note that while the charge-to-mass ratios considered here ($10^{-4} \lesssim \alpha \lesssim 10^{-3}$) are larger than those discussed in [37], they remain well below the thresholds required to induce detectable modifications to gravitational-wave waveforms [41]. Consequently, this scenario remains fully consistent with current gravitational-wave constraints.

tion to the tidal-disruption-favorable mass ratio regime, in Sec. III A.

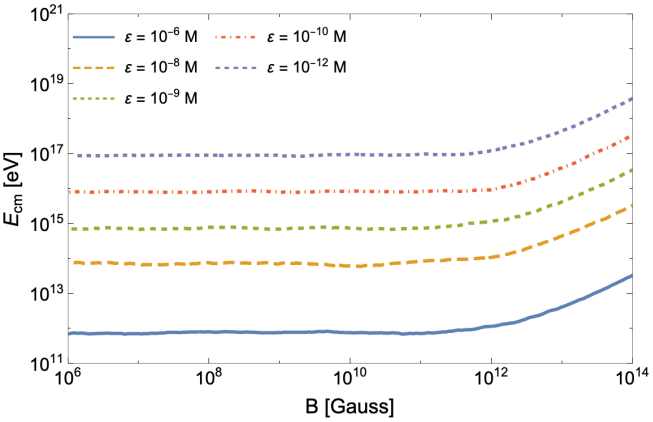
Finally, we note that BNS remnants occupy a mass range, $M \sim 2.5$–$4.5\,M_\odot$, well below the 20–150 $M_\odot$ range considered for the BBH population above. No BNS event is therefore included in Table I, and any reference to BNS magnetic field strengths elsewhere in this work (e.g. Fig. 2) should be understood as illustrative of the neutron-star magnetospheric field regime, not corresponding to the higher BBH remnant masses shown in that figure.

III. RESULTS AND DISCUSSION

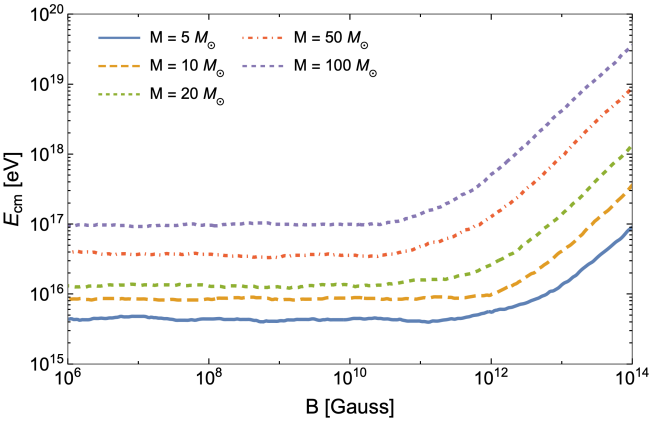
In this section, we explore in more detail the parameter space of center–of–mass collisions around magnetized Kerr black holes in the regime relevant for compact binaries that will be observed as GW sources. Using the framework described in Sec. II, we compute the center–of–mass energy $E_{\rm cm}$ of proton–proton collisions at a radius $r = r_{\rm H} + \varepsilon$ outside the event horizon, for a range of magnetic fields B, black–hole masses M, spin parameters a/M, and specific angular momenta ℓ_1 and ℓ_2 of the colliding particles. We stress that UHECR observations tend to favor heavier incoming particles. In our scenario, this corresponds to larger m_0, which would simply increase $E_{\rm max}$. Hence, adopting protons as the primary particles should be regarded as a conservative choice.

Figure 1-(a) shows $E_{\rm cm}$ as a function of the magnetic field for a fixed mass $M = 10\,M_\odot$ and spin $\chi_f = 0.9$, varying the radial offset in the interval $\varepsilon = (10^{-6} - 10^{-12})M$. For weak fields, $B \lesssim 10^{11}$ G, the dependence on ε is modest, with $E_{\rm cm}$ ranging between $\sim 10^{12}$ and 10^{16} eV as the collision point is moved closer to the horizon. For stronger fields, $B \gtrsim 10^{12}$ G, the effect of the radial offset becomes more pronounced and the curves separate: collisions occurring at $\varepsilon \lesssim 10^{-10}M$ reach $E_{\rm cm} \gtrsim 10^{18}$ eV, whereas for $\varepsilon \sim 10^{-6}M$ they remain below the ultrahigh–energy regime. This behaviour confirms that the magnetic BSW mechanism becomes most efficient when collisions take place very close to the horizon and in the presence of strong magnetic fields, but it also shows that the threshold in ε is not extremely fine–tuned: once $\varepsilon \lesssim 10^{-10}M$ the curves nearly saturate and the gain in $E_{\rm cm}$ with further inward displacement is relatively small.

The apparent bumpiness in Figs. 1-(a) and (b) for $B \lesssim 10^{12}$ G is a sampling artefact of the numerical optimization over (ℓ_1, ℓ_2). In the gravity-dominated regime, the energy landscape is relatively flat but punctuated by narrow resonant ridges (visible in Fig. 4(a)); small changes in B shift these ridges, causing the discrete grid to jump between ridge peaks and the surrounding plateau. For $B \gtrsim 10^{12}$ G, the magnetic term dominates and the effective potential becomes smoother, yielding correspondingly smooth curves. The envelope of achievable energies is monotonically increasing with B.



(a) $E_{\rm cm}$ as a function of B for different radial offsets ε at fixed $M = 10\,M_\odot$, $\chi_f = 0.9$, $\ell_1 = 1.5$ and $\ell_2 = -1.5$.



(b) $E_{\rm cm}$ as a function of B for different masses at fixed $\varepsilon = 10^{-10}M$, $\chi_f = 0.9$, $\ell_1 = 1.5$ and $\ell_2 = -1.5$.

FIG. 1: Center-of-mass energy $E_{\rm cm}$ of proton–proton collisions near a magnetised Kerr black hole as a function of the magnetic field B. Panel (a) shows the dependence on the radial offset ε from the horizon, while panel (b) shows the dependence on the black-hole mass M.

The impact of the black–hole mass is illustrated in Fig. 1-(b), where we fix $\varepsilon = 10^{-10}M$, $\chi_f = 0.9$, and the angular momenta $\ell_1 = 1.5$ and $\ell_2 = -1.5$, and vary the mass from $M = 5$ to $100\,M_\odot$. For $B \sim 10^{10}$ G all masses yield $E_{\rm cm} \sim 10^{16}$–10^{17} eV, while for $B \sim 10^{14}$ G the most massive systems reach $E_{\rm cm} \sim 10^{19}$–10^{20} eV. The nearly parallel curves indicate an approximate scaling $E_{\rm cm} \propto M$ at fixed $(B, \varepsilon, \chi_f, \ell_i)$, as already suggested by the analytic expression for the form factor $\mathcal{F}(\chi_f, \mathcal{B}, \ell_1, \ell_2)$. This implies that the most massive stellar–origin black holes observed in current GW catalogs are naturally favored as sources of the highest–energy events, but even systems with $M \lesssim 20\,M_\odot$ can produce $E_{\rm cm} \gtrsim 10^{18}$ eV provided that $B \gtrsim 10^{13}$ G and collisions occur sufficiently close to the horizon.

To better visualize the relative contribution of the magnetic field to particle acceleration, Fig. 2 presents the magnetic amplification factor $E_{\rm cm}(B)/E_{\rm cm}(0)$, which quantifies how many times the presence of a magnetic

field enhances the collision energy compared to the purely gravitational BSW mechanism (i.e., $B = 0$). We adopt representative parameters $M = 50\,M_\odot$, $\chi_f = 0.9$, $\varepsilon = 10^{-10}M$, and $\ell_1 = 1.5$, $\ell_2 = -1.5$, which correspond to a near-extremal black hole with collisions occurring very close to the horizon. The horizontal dashed line at ratio = 1 marks the baseline energy where the magnetic field has no effect, serving as a reference to identify three distinct acceleration regimes.

In the *gravity-dominated regime* ($B < 10^{12}$ G), the amplification factor remains below ~ 2, indicating that the magnetic field provides at most a modest enhancement over the purely gravitational mechanism. Here, particle acceleration is driven primarily by the spacetime curvature near the event horizon, with magnetic effects playing a secondary role. This regime is consistent with environments where magnetic fields are relatively weak or the collision geometry does not favor strong Lorentz-force contributions.

As the magnetic field strength increases into the *transition regime* ($10^{12}\,\mathrm{G} \lesssim B \lesssim 10^{13}\,\mathrm{G}$), the amplification factor rises steeply from ~ 2 to ~ 5. In this interval, magnetic and gravitational effects become comparable, and the collision energy becomes increasingly sensitive to the field strength. Notably, this range includes typical magnetic-field values inferred for BH-NS and NS-NS merger environments ($B \sim 10^{12}$ G, marked by the purple vertical line), where post-merger outflows and magnetospheric reconnection can naturally generate strong fields [e.g., 35, 36]. The fact that realistic NS field strengths fall squarely within this transition regime suggests that magnetic enhancement of BSW collisions may be a generic feature of mergers involving NSs, rather than an exotic or fine-tuned scenario.

For $B > 10^{13}$ G, the system enters the *magnetic-dominated regime*, where the amplification factor exceeds ~ 5 and approaches ~ 10 at $B \sim 10^{14}$ G indicating magnetar-strength fields. In this regime, the magnetic field overwhelms the gravitational contribution and becomes the dominant driver of particle acceleration. The tenfold enhancement implies that collisions which would yield $E_{\rm cm} \sim 10^{19}$ eV in the absence of a magnetic field can reach $E_{\rm cm} \sim 10^{20}$ eV when $B \sim 10^{14}$ G. This places the collision energies well into the UHECR regime. While magnetar-strength fields are less common than typical BNS and BH-NS merger fields, they may occur transiently during the most violent phases of compact binary coalescence or in the immediate vicinity of newly formed hypermassive neutron stars [e.g., 43, 49].

The three-regime structure revealed in Fig. 2 has important implications for identifying astrophysical sources of UHECRs. First, it demonstrates that magnetic fields do not need to reach extreme values to significantly enhance particle acceleration: even moderate fields of $B \sim 10^{12}$–10^{13} G, which are well within the range of current numerical simulations of BNS mergers, can double or triple the collision energy. Second, the rapid transition from the gravity-dominated to the magnetic-dominated regime occurs over a relatively narrow range in $\log_{10}(B)$, suggesting that observations of UHECRs correlated with gravitational-wave events could place strong constraints on the magnetic-field strengths in these systems. Finally, the figure underscores the robustness of the magnetic BSW mechanism: unlike the original BSW scenario, which required extremely fine-tuned parameters to achieve unbounded energies, the presence of even moderately strong magnetic fields enables UHECR production across a broad range of astrophysically realistic configurations. It is important to emphasize that $B \sim 10^{12}$ G does not redefine the threshold for ultra-high-energy particle production obtained in our previous work [37]. Fields of order $10^{10} - 10^{12}$ G remain sufficient to generate UHECR-scale collision energies. The transition identified here instead marks the point at which magnetic effects become the dominant contribution to the center-of-mass energy, providing a refined physical interpretation of the acceleration mechanism.

To visualize the global structure of the parameter space, in Fig. 3 we present contour maps of $\log_{10}(E_{\rm cm}/\mathrm{eV})$. In both panels, we adopt the near–horizon radius $r = r_{\rm H} + \varepsilon$ with $\varepsilon = 10^{-10}M$ and the same angular momenta $\ell_1 = 1.5$ and $\ell_2 = -1.5$. Figure 3-(a) spans the plane $(\log_{10} B, \log_{10} M)$ at fixed spin $\chi_f = 0.9$. The contours are almost vertical for $B \lesssim 10^{11}$ G, indicating a weak dependence on B and a mild increase of $E_{\rm cm}$ with mass. At $B \gtrsim 10^{12}$ G the contours bend and $E_{\rm cm}$ rises steeply, surpassing 10^{18} eV for $M \gtrsim 20\,M_\odot$ and approaching 10^{20} eV for $M \sim 100\,M_\odot$ and $B \sim 10^{14}$ G. This plot shows a broad region of parameter space in which ordinary neutron–star magnetospheric fields or fields sourced by small charge–to–mass ratios of the black holes are sufficient to drive ultra-high–energy collisions in systems compatible with current GW observations.

The horizontal band structures in Fig. 3-(a) have the same origin as the bumpiness in Figs. 1, but they manifest along the mass axis. As M varies, the allowed (ℓ_1, ℓ_2) range shifts, causing the resonant ridges in angular-momentum space to drift. At certain masses, the optimal configuration aligns with a critical trajectory near the horizon, temporarily elevating $E_{\rm cm}$ above the smooth trend. Between these masses, the grid falls between ridges and records a lower value. These deviations are expected artifacts of the finite angular-momentum grid.

Figure 3-(b) explores instead the $(\log_{10} B, \chi_f)$ plane for a fixed mass $M = 50\,M_\odot$. For $B \lesssim 10^{11}$ G the dependence on the spin parameter is weak: $E_{\rm cm}$ varies by less than an order of magnitude when χ_f is changed from 0.5 to nearly extremal values, remaining below 10^{18} eV. In contrast, when $B \gtrsim 10^{12}$ G the contours become more tilted, and both higher spin and stronger magnetic fields contribute to increasing $E_{\rm cm}$. Ultrahigh–energy collisions appear already for $\chi_f \simeq 0.6$–0.7 at $B \sim 10^{13}$ G and extend up to $E_{\rm cm} \gtrsim 10^{19}$ eV for nearly extremal spins and $B \sim 10^{14}$ G. Compared with the original BSW scenario, which required fine–tuning to $\chi_f \to 1$, the presence of

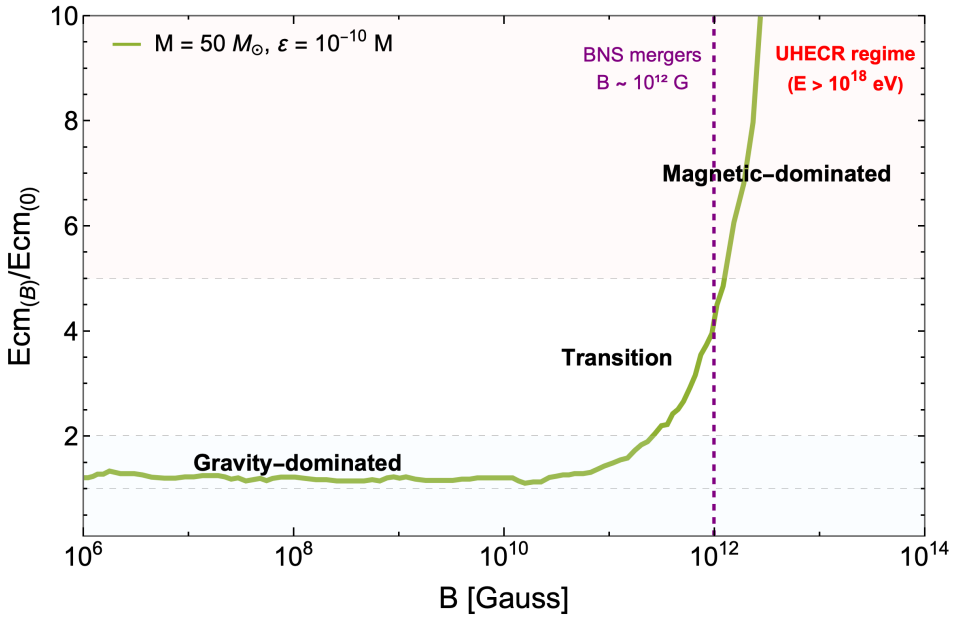


FIG. 2: Magnetic amplification factor $E_{\rm cm}(B)/E_{\rm cm}(0)$ for proton–proton collisions near a Kerr black hole ($M = 50\,M_\odot$, $\chi_f = 0.9$, $\varepsilon = 10^{-10}M$, $\ell_1 = 1.5$, $\ell_2 = -1.5$) as a function of magnetic field strength B. The horizontal line at ratio = 1 marks the baseline BSW energy (no magnetic enhancement). Three regimes are visible: gravity-dominated ($B < 10^{12}$ G), transition (10^{12} G $\lesssim B \lesssim 10^{13}$ G), and magnetic-dominated ($B > 10^{13}$ G). The vertical dashed line indicates a fiducial magnetospheric field strength of $B \sim 10^{12}$ G, relevant for charged BH-BH remnants of comparable mass; this panel does not represent a BNS remnant, whose typical mass (~ 2.5–$4.5\,M_\odot$) lies well outside the range considered here. For $B \gtrsim 10^{13}$ G, magnetic fields amplify collision energies by nearly an order of magnitude, enabling UHECR production ($E > 10^{18}$ eV) in astrophysically realistic scenarios.

a magnetic field therefore dramatically enlarges the allowed range of spin parameters: for realistic B, the production of UHE events is possible for almost the entire distribution of spins inferred from GW catalogs.

Finally, Fig. 4 presents contour maps of $\log_{10}(E_{\rm cm}/{\rm eV})$ in the (ℓ_1, ℓ_2) plane for a magnetised Kerr black hole with $M = 50\,M_\odot$, $\chi_f = 0.9$ and $\varepsilon = 10^{-10}M$, for two representative magnetic-field strengths, $B = 10^{12}$ G [panel (a)] and $B = 10^{14}$ G [panel (b)]. In both cases we explore $\ell_i \in [-2.63, 2.63]$, and the maps exhibit a patchy pattern of narrow ridges and islands, corresponding to local maxima of $E_{\rm cm}$ where the particle orbits approach critical trajectories. The red dashed diagonal marks $\ell_1 = \ell_2$, along which the configuration is symmetric under the exchange of the two particles, while the white dashed lines indicate $\ell_1 = 0$ and $\ell_2 = 0$. For $B = 10^{12}$ G the dynamic range is relatively modest, with $\log_{10}(E_{\rm cm}/{\rm eV}) \simeq 17.1$–$17.3$ across most of the plane, and broad regions around $\ell_1 \approx 0$ and $\ell_2 \approx 0$ already yielding $E_{\rm cm} \gtrsim 10^{17}$ eV. Increasing the field to $B = 10^{14}$ G shifts the entire pattern upward by about two orders of magnitude so that typical configurations reach $E_{\rm cm} \sim 10^{19}$ eV, and the highest ridges slightly exceed this value. These maps show that, once the magnetic field, mass, spin and radial offset are chosen in the UHE–favourable regime, ultrahigh–energy collisions do not rely on extremely fine–tuned angular momenta: while the very highest energies are associated with special combinations of (ℓ_1, ℓ_2), a broad portion of phase space produces $E_{\rm cm}$ within an order of magnitude of the extrema.

The island structure visible in Fig. 4 reflects the genuine topology of the BSW energy functional. The $E_{\rm cm}$ exhibits sharp, localized maxima near critical angular-momentum values ($\ell_{\rm crit} \approx 2$) where particles approach the horizon asymptotically, departing from these values causes a rapid energy drop. The feasibility constraint $\dot{r}^2 \geq 0$ (Eq. (14)) further excludes angular-momentum combinations corresponding to trapped trajectories, carving out disconnected viable regions. The magnetic field introduces additional families of critical orbits via its B-dependent shift of the effective potential, redistributing the island pattern, as seen comparing panels (a) and (b). The absence of smooth variation thus reflects the highly non-linear, multi-peaked structure of $E_{\rm cm}(\ell_1, \ell_2)$ in Kerr spacetime.

To connect our theoretical framework with actual gravitational wave observations, we apply our calculations to the complete catalog of high-spin merger remnants detected by LIGO-Virgo-KAGRA. Table I lists all 34 gravitational wave events from the GWTC-2.1, GWTC-3, and GWTC-4.0 catalogs with final spin parameters exceeding $\chi_f > 0.7$ [38–40]. For each event, we report the redshift z, the component masses before merger (m_1 and m_2), the final remnant mass M, the final dimensionless spin χ_f, and our computed maximum center-of-mass energy $\log_{10}(E_{\rm max}\ [{\rm eV}])$ assuming collisions at $\varepsilon = 10^{-10}M$

from the horizon with magnetic field $B = 10^{14}$ G and optimized angular momenta within the physically allowed range given by Eq. 17.

The predicted maximum energies span approximately three orders of magnitude, from $\log_{10}(E_{\rm max}) \approx 17.8$ for the lowest-mass, lowest-spin systems to $\log_{10}(E_{\rm max}) \approx 20.2$ for the most massive, highest-spin events. The highest predicted energy corresponds to GW200308_173609, with a final mass $M = 88^{+169}_{-47}\,M_\odot$ and spin $\chi_f = 0.91^{+0.03}_{-0.08}$, yielding $E_{\rm max} \sim 1.6 \times 10^{20}$ eV. This places it at the extreme end of the observed UHECR spectrum. Other notable high-energy events include GW190519_153544 ($E_{\rm max} \sim 10^{20}$ eV, $M = 100.0^{+13.0}_{-12.9}\,M_\odot$, $\chi_f = 0.79^{+0.07}_{-0.13}$) and GW190706_222641 ($E_{\rm max} \sim 7.9 \times 10^{19}$ eV, $M = 107.3^{+25.2}_{-15.9}\,M_\odot$, $\chi_f = 0.78^{+0.09}_{-0.18}$).

The distribution of predicted energies reflects both the mass and spin distributions of the observed merger population. Events with final masses below $\sim 30\,M_\odot$ typically produce maximum energies below the UHECR threshold of 10^{18} eV even at our fiducial field strength, while systems with $M \gtrsim 50\,M_\odot$ and $\chi_f \gtrsim 0.75$ consistently achieve energies in the UHECR regime. The approximate linear scaling $E_{\rm max} \propto M$ evident in Fig. 1-(b) is clearly visible in the catalog: comparing events with similar spins but different masses, such as GW151226 ($M \approx 21\,M_\odot$, $\log_{10} E_{\rm max} = 18.05$) and GW170729 ($M \approx 80\,M_\odot$, $\log_{10} E_{\rm max} = 19.56$), shows that a factor of ~ 4 increase in mass produces approximately a factor of ~ 30 increase in maximum energy, consistent with the mass scaling and the implicit spin dependence through the amplification function $\mathcal{F}$.

Notably, the sole binary neutron star event in our catalog, GW170817, has upper limits of $M \leq 2.8\,M_\odot$ and $\chi_f \leq 0.89$ that would place it well below the UHECR regime for our assumed magnetic field strength. However, BNS mergers may feature substantially different magnetic field configurations and particle injection mechanisms compared to BBH systems, making direct comparison problematic. The absence of confirmed BH-NS mergers with $\chi_f > 0.7$ in the current catalog prevents us from making specific predictions for this particularly promising class of UHECR sources, though our general framework applies equally well once such systems are detected and characterized.

Taken together, these results reinforce and extend the picture presented in our previous Letter [37]: magnetised compact binaries are natural sites for accelerating particles to ultrahigh energies via the magnetic BSW mechanism. For typical parameters of charged BH-BH systems with masses $M \sim 10$–$100\,M_\odot$, or BH-NS systems in the disruption-favorable mass ratio regime ($M_{\rm BH} \lesssim 7\,M_\odot$), magnetic fields in the range $B \sim 10^{11}$–10^{13} G are sufficient to produce $E_{\rm cm} \gtrsim 10^{18}$ eV over a wide range of spins and particle angular momenta. This robustness with respect to source parameters suggests that UHECR production in compact–binary mergers could be a generic phenomenon rather than a rare, fine–tuned occurrence, and motivates detailed studies of particle escape and propagation, as well as joint UHECR–GW searches, to further test this scenario.

A. Astrophysical viability of the magnetic BSW mechanism in BNS post-merger environments

A natural extension of this work is the post-merger production of UHECRs in binary neutron-star coalescences. Unlike the pre-merger phase, this channel relies on the formation of a metastable, often differentially rotating and strongly magnetized neutron-star remnant, or its subsequent collapse into a black hole [50, 51]. We acknowledge that a passive vacuum dipole decay (r^{-3}) from a companion would require non-physical surface fields for high-mass systems. However, in realistic merger and post-merger environments, the magnetic flux is "anchored" by high-conductivity plasma, baryon-loaded ejecta, and accretion debris [52, 53]. This flux anchoring mechanism maintains high field densities in the near-horizon region independently of the companion's initial dipole distance, providing the necessary physical framework to sustain the required field strengths. Whether sourced by flux inherited from the remnant or amplified by disk-driven MHD processes [54], the black hole's ergosphere remains a viable site for particle acceleration. We stress that the disk-anchored field argument above applies only to BH-NS systems in the disruption-favorable regime, $q \equiv M_{\rm BH}/M_{\rm NS} \lesssim 5$, i.e. $M_{\rm BH} \lesssim 7\,M_\odot$ for a $1.4\,M_\odot$ companion, even at near-extremal spin [55]. For the more massive remnants populating Table I ($M \sim 20$–$150\,M_\odot$), the mass ratio is far too large for tidal disruption to occur, no disk forms, and the relevant field-sustaining mechanism there is instead the charge-to-mass ratio scenario for BH-BH systems described above, or fields inherited directly from residual accretion in the pre-merger phase. We therefore do not invoke post-merger disk formation for the BBH population analyzed in Table I.

The availability of charged particles is ensured by baryon-loaded ejecta, fallback material, and disk/wind outflows, which provide a copious plasma reservoir for injection into the ergosphere. While transient, these magnetic configurations may persist long enough to be astrophysically significant, depending on the survival time of the accretion disk and reconnection timescales [56]. Furthermore, if the collapse to a black hole is delayed, magnetic-field amplification mechanisms operating in the hypermassive neutron-star remnant can significantly increase the field strength prior to collapse. Kelvin–Helmholtz instabilities generated during merger and magnetorotational-instability-driven turbulence in the remnant and accretion flow are known to amplify magnetic fields by several orders of magnitude [42–45]. GRMHD simulations have reported magnetic-field strengths reaching magnetar levels ($\sim 10^{15}$ G) and, in some regions, even larger values [45, 46, 48]. The newly

formed black hole may therefore be embedded in an environment considerably more magnetized than the original neutron stars. This motivates a dual-stage (pre- and post-merger) acceleration framework that would be falsifiable via multimessenger observations [57].

The background metric can be treated as effectively stationary throughout the process. For a $150M_\odot$ black hole, the light-crossing times are on the millisecond scale, which is perfectly compatible with the ultra-relativistic interaction and escape timescales of the BSW mechanism. There is a clear hierarchy of timescales: the spacetime settles into a stationary state over the damping time ($\tau_{QNM} \approx 0.15$ ms for $3M_\odot$, scaled proportionally for higher masses) [58, 59], while the magnetic configuration anchored by the disk persists for $\tau_{disk} \sim 0.1$ to 1 s [51]. Since $\tau_{disk} \gg \tau_{QNM}$, the "accelerator" remains active and stable for a duration orders of magnitude longer than the final plunge dynamics, providing a robust physical environment for UHECR production even in high-mass remnants where linear mass scaling ($E_{max} \propto M$) compensates for more conservative field strengths. Further analysis of the above points is left for future work.

IV. SUMMARY AND CONCLUSIONS

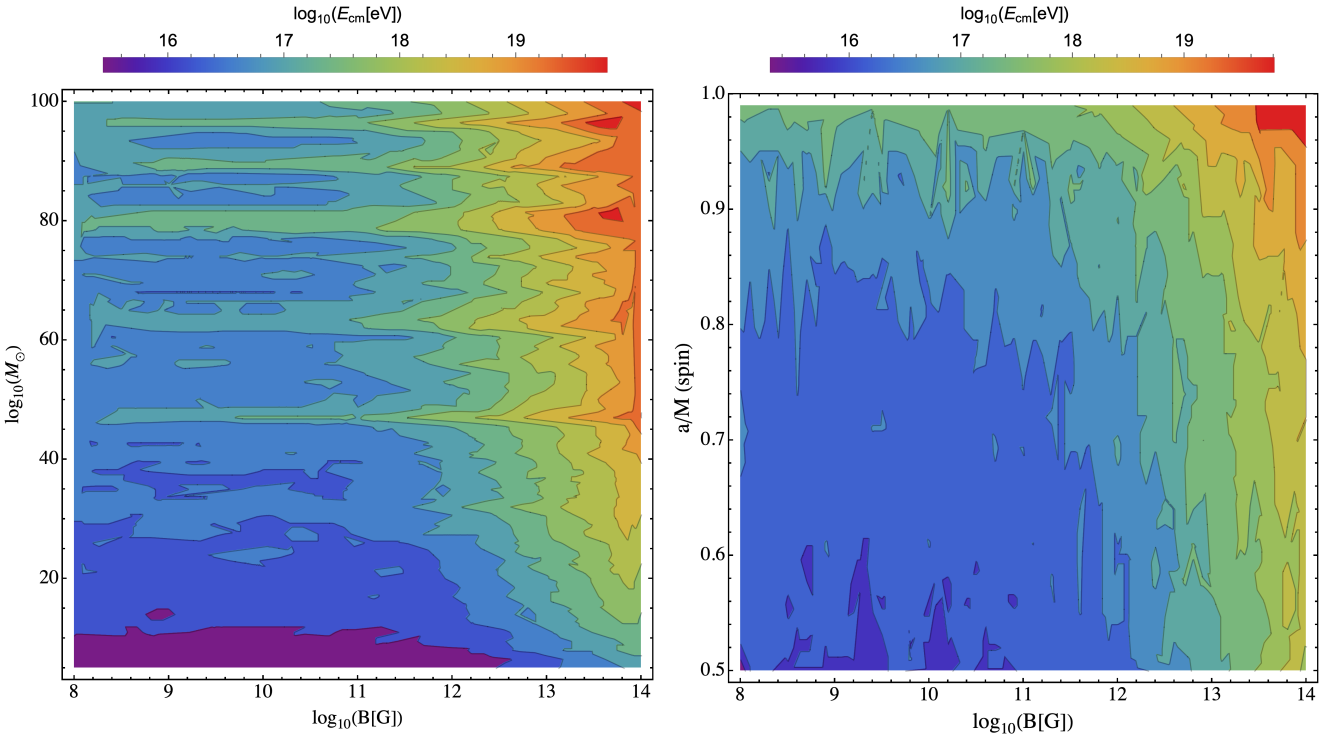
We have investigated UHE particle production through the magnetized BSW mechanism in BH–NS binaries, BH–BH binaries in which at least one component has a charge-to-mass ratio of $\sim 10^{-4}$–10^{-3}, or post-merger BH remnants formed in binary NS mergers detected by LIGO-Virgo-KAGRA. By solving the geodesic equations for charged particles in magnetized Kerr spacetime, we demonstrate that binary coalescences represent viable astrophysical sources of ultra-high-energy cosmic rays.

Our previous Letter [37] demonstrated that magnetic fields exceeding approximately $10^{10} - 10^{12}$ G are sufficient to enable ultra-high-energy particle production in compact-binary environments. The present work extends that analysis by systematically investigating how the acceleration efficiency evolves as the magnetic field strength increases. In particular, we identify a transition toward a magnetic-dominated regime for fields approaching 10^{12} G and quantify the resulting enhancement up to $B \sim 10^{14}$ G. Therefore, the present results should be viewed as a refinement and extension of the original framework rather than a modification of its conclusions.

The presence of strong magnetic fields in the immediate vicinity of the event horizon enhances the center-of-mass energy. It scales as $E_{\rm max} = m_0c^2(M/M_\odot)\mathcal{F}(\chi_f, \mathcal{B}, \ell_1, \ell_2)$, where the amplification function $\mathcal{F}$ depends on black hole spin χ_f, normalized magnetic field strength $\mathcal{B}$, and particle angular momenta. For merger remnants with masses $M \sim 20$–$150\,M_\odot$ (characteristic of the BBH population), spins $\chi_f \sim 0.7$–0.9, and magnetic fields $B \sim 10^{12}$–10^{14} G, we find maximum achievable energies spanning $E_{\rm max} \sim 10^{17}$–10^{20} eV, placing these systems squarely in the UHECR regime.

Our systematic parameter space exploration reveals three distinct acceleration regimes characterized by magnetic field strength, see Fig. 2. In the gravity-dominated regime ($B < 10^{12}$ G), magnetic fields provide only modest enhancement, with amplification factors below ~ 2, and particle acceleration is driven primarily by spacetime curvature. As field strength increases into the transition regime (10^{12} G $\lesssim B \lesssim 10^{13}$ G), magnetic and gravitational effects become comparable, with amplification factors rising steeply to ~ 5. This transition regime is particularly significant because it encompasses field strengths naturally expected in binary neutron star mergers, suggesting that magnetic enhancement of the BSW mechanism may be a generic feature rather than requiring fine-tuned conditions. In the magnetic-dominated regime ($B > 10^{13}$ G), corresponding to magnetar-strength fields, amplification factors approach ~ 10 and the magnetic field becomes the dominant driver of particle acceleration.

A crucial finding is that magnetic fields dramatically broaden the viable parameter space compared to the original BSW scenario. While the vacuum BSW mechanism required extreme fine-tuning to near-extremal spins ($\chi_f \to 1$) [21], the presence of magnetic fields $B \gtrsim 10^{12}$



(a) Contour map of $\log_{10}(E_{\rm cm})$ as a function of $\log_{10}(B)$ and $\log_{10}(M/M_\odot)$ for particle collisions.

(b) Contour map of $\log_{10}(E_{\rm cm})$ as a function of $\log_{10}(B)$ and the spin parameter χ_f for the same setup.

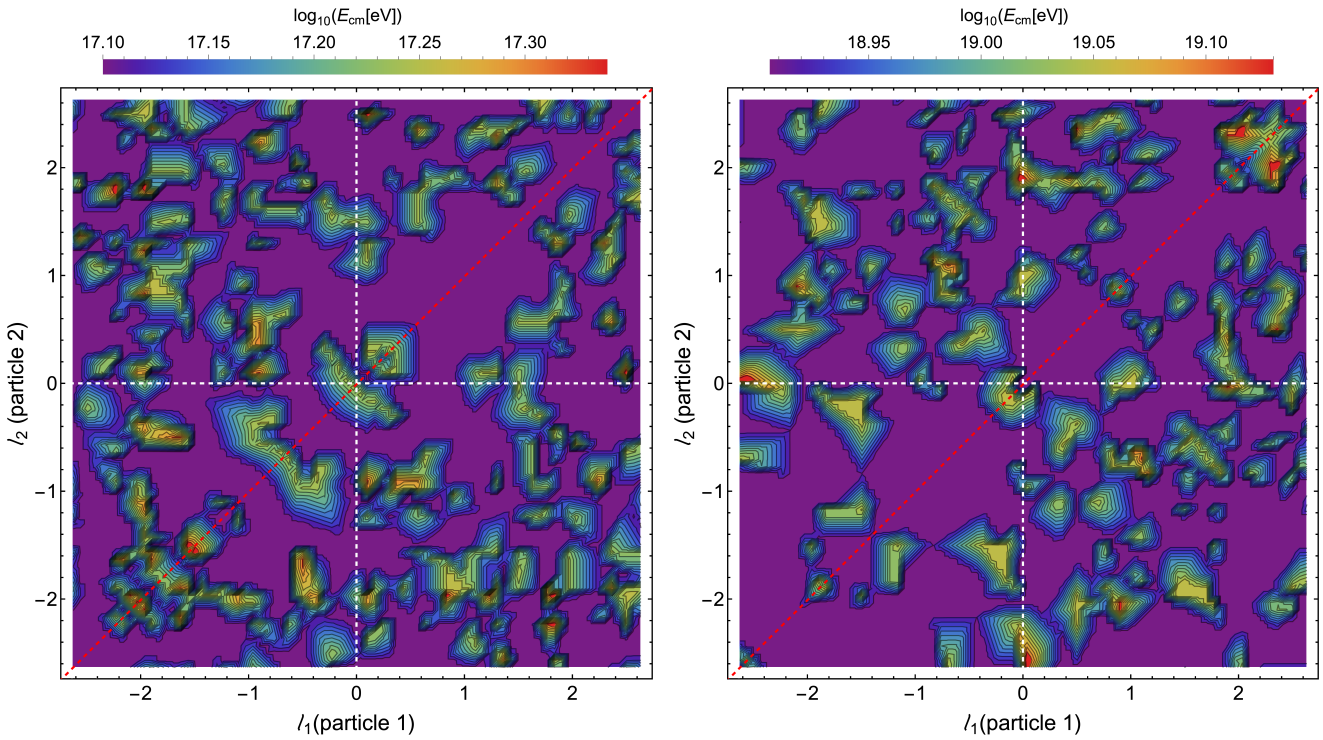
FIG. 3: Contour maps of the center-of-mass energy $E_{\rm cm}$ for proton–proton collisions close to the horizon of a magnetised Kerr black hole, in a regime relevant for stellar-mass black holes involved in gravitational-wave mergers. In both panels we adopt a fixed radial offset $r = r_{\rm H} + \varepsilon$ with $\varepsilon = 10^{-10}M$ and specific angular momenta $\ell_1 = 1.5$ and $\ell_2 = -1.5$. Colours indicate $\log_{10}(E_{\rm cm}\,[\rm eV])$. Panel (a) shows the dependence on magnetic-field strength and black-hole mass for spin $\chi_f = 0.9$, whereas panel (b) shows the dependence on magnetic-field strength and spin for a fixed mass $M = 50\,M_\odot$.

G enables UHE particle production across nearly the entire distribution of spins observed in gravitational wave catalogs ($\chi_f \gtrsim 0.7$). This eliminates the most severe astrophysical objection to the BSW mechanism and transforms it from a theoretical curiosity into a potentially realistic acceleration process operating in compact binary mergers.

Applying our framework to the catalog of 34 high-spin gravitational wave events detected through GWTC-2, GWTC-3 and preliminary GWTC-4 observations, we find that systems with $\chi_f \gtrsim 0.85$ and $M \gtrsim 100\,M_\odot$ can reach $E_{\rm max} \sim 10^{20}$ eV at our fiducial magnetic field strength $B = 10^{14}$ G, while typical events with $\chi_f \sim 0.7$–0.8 and $M \sim 50$–$70\,M_\odot$ achieve $E_{\rm max} \sim 10^{18}$–10^{19} eV, see Table I. These event-by-event predictions establish direct, testable correlations between gravitational wave observables and UHECR production efficiency.

Our calculations adopt simplified assumptions including equatorial particle orbits and a uniform magnetic field configuration with $A_\phi = Bg_{\phi\phi}/2$. More realistic treatments incorporating full three-dimensional magnetospheric geometry from magnetohydrodynamic simulations may modify quantitative predictions while preserving the qualitative picture. The origin and magnitude of magnetic fields in binary black hole mergers remains uncertain, though our fiducial value $B = 10^{14}$ G represents a plausible upper estimate based on scaling arguments. Lower field strengths in the range 10^{12}–10^{13} G, more readily achieved through residual accretion or transient merger effects, still enable UHECR production for favorable parameter combinations. We have focused on collision energies near the horizon without detailed modeling of particle escape, propagation through the merger environment, or energy losses during transit to Earth. A complete assessment requires incorporating these effects along with realistic particle injection mechanisms and composition modeling.

The prospects for testing this scenario through multi-messenger observations are promising. Third-generation gravitational wave detectors such as Cosmic Explorer [60] and Einstein Telescope [61] will detect binary mergers with unprecedented precision, resolving remnant properties to percent-level accuracy and enabling detailed predictions for individual events. Simultaneously, next-generation cosmic ray observatories will improve mass composition measurements and directional resolution, potentially enabling coincident detection of UHECRs with gravitational wave sources [62–65]. The detection or



(a) $B = 10^{12}$ G (b) $B = 10^{14}$ G

FIG. 4: Contour map of $\log_{10}(E_{\rm cm}\,[\rm eV])$ as a function of the specific angular momenta of the two colliding particles, ℓ_1 (particle 1) and ℓ_2 (particle 2). The collisions occur near the horizon at $r = r_{\rm H} + \varepsilon$ with $\varepsilon = 10^{-10}M$ for a magnetised Kerr black hole of mass $M = 50\,M_\odot$, spin parameter $\chi_f = 0.9$, and magnetic field $B = 10^{12}$ G. White dashed lines indicate $\ell_1 = 0$ and $\ell_2 = 0$, while the red dashed diagonal marks $\ell_1 = \ell_2$, along which the configuration is symmetric under the exchange of the two particles.

non-detection of UHECRs correlated with specific merger events would provide powerful constraints on magnetic field strengths and particle acceleration efficiency in these extreme environments.

In conclusion, the present work should be viewed as a natural extension of our previous study [37]. In that Letter, we demonstrated that astrophysically realistic magnetic fields larger than $\sim 10^{10} - 10^{12}$ G in the vicinity of black hole event horizons are already sufficient to trigger ultra-high-energy particle production. Here, we go beyond that initial result by identifying distinct acceleration regimes and quantifying the transition from gravity-dominated to magnetic-dominated dynamics, which occurs for magnetic fields $B \gtrsim 10^{12}$ G. These results do not alter the original conclusion; rather, they provide a deeper physical understanding of the mechanism and clarify how its efficiency evolves as the magnetic field strength increases. Taken together, the results of both studies strengthen the case that compact binary mergers embedded in strongly magnetized environments constitute theoretically robust and astrophysically plausible sources of ultra-high-energy cosmic rays. The inclusion of realistic magnetic fields transforms the BSW mechanism from requiring extreme fine-tuning to being a potentially generic feature of compact binary coalescences. Our quantitative predictions linking gravitational wave observables to particle acceleration efficiency provide a concrete framework for multi-messenger searches that could transform our understanding of the most energetic particles in the universe.

V. ACKNOWLEDGMENTS

The authors acknowledge the support of the NAPI "Fenômenos Extremos do Universo" of Fundação de Apoio à Ciência, Tecnologia e Inovação do Paraná. C.H.C.-A. research is supported by Araucária Foundation (337/2025) and COFPI/PRPI/UFPR (20/2025). R.C.A. research is supported by CNPq (308859/2025-1) and (4000045/2023-0), Araucária Foundation (698/2022) and (721/2022) and FAPESP (2021/01089-1). The authors acknowledge the AWS Cloud Credit/CNPq and the National Laboratory for Scientific Computing (LNCC/MCTI, Brazil) for providing HPC resources of the SDumont supercomputer, which have contributed to the research results reported in this paper. URL: https://sdumont.lncc.br. J.G.C. is grateful for the support of FAPES (1020/2022, 1081/2022, 976/2022, 332/2023, 1514/2025), CNPq (311758/2021-5,

TABLE I: List of LIGO-Virgo-KAGRA sources with rotational parameter $\chi_f \equiv a/M \equiv J/M^2 > 0.7$ (J is the BH's angular momentum) for the BH produced after the merger of BBHs/BH-NS/BNS. Updated with latest GWTC-2.1, GWTC-3, and GWTC-4.0 measurements. The list is ordered following the chronological detections. The masses of the BHs/NSs before the merger are denoted by m_1 and m_2, and M is the mass of the final BH/NS. All masses are in solar mass ($M_\odot$) units. The redshift of a source is z. $\log_{10} E$ is the maximum center-of-mass energy (in eV) for particle collisions at $\varepsilon = 10^{-10}M$ from the horizon, calculated using the BSW mechanism with magnetic field $B = 10^{14}$ G and optimal angular momenta within the allowed range $-2(1+\sqrt{1-\chi_f}) < \ell < 2(1+\sqrt{1-\chi_f})$. The events are classified here as binary of black holes (BBHs) or binary of black hole-neutron star (BH-NS) or binary of neutron stars (BNSs).

Catalog	Event	z	m_1	m_2	M	χ_f	$\log_{10} E$	Type
GWTC-2.1	GW151226	$0.10^{+0.03}_{-0.04}$	$14.2^{+11.1}_{-3.6}$	$7.5^{+2.4}_{-2.8}$	$20.7^{+8.6}_{-1.6}$	$0.74^{+0.07}_{-0.05}$	18.05	BBH
GWTC-2.1	GW170729	$0.44^{+0.24}_{-0.19}$	$54.7^{+12.7}_{-12.8}$	$30.2^{+11.9}_{-10.2}$	$80.3^{+13.5}_{-10.2}$	$0.81^{+0.07}_{-0.13}$	19.56	BBH
GWTC-2.1	GW170814	$0.13^{+0.03}_{-0.05}$	$30.9^{+5.4}_{-3.3}$	$24.9^{+3.0}_{-4.0}$	$53.2^{+3.2}_{-2.7}$	$0.72^{+0.07}_{-0.05}$	18.91	BBH
GWTC-2.1	GW170817*	$0.01^{+0.00}_{-0.00}$	$1.46^{+0.12}_{-0.10}$	$1.27^{+0.09}_{-0.09}$	≤ 2.8	≤ 0.89	–	BNS
GWTC-2.1	GW170823	$0.36^{+0.13}_{-0.15}$	$38.3^{+9.5}_{-6.2}$	$29.0^{+6.5}_{-7.8}$	$63.9^{+9.6}_{-6.8}$	$0.72^{+0.09}_{-0.12}$	19.06	BBH
GWTC-2.1	GW190517_055101	$0.33^{+0.26}_{-0.15}$	$39.2^{+13.9}_{-9.2}$	$24.0^{+7.4}_{-7.9}$	$60.1^{+9.9}_{-9.4}$	$0.87^{+0.05}_{-0.07}$	19.14	BBH
GWTC-2.1	GW190519_153544	$0.45^{+0.24}_{-0.15}$	$65.1^{+10.8}_{-11.0}$	$40.8^{+11.5}_{-12.7}$	$100.0^{+13.0}_{-12.9}$	$0.79^{+0.07}_{-0.13}$	20.05	BBH
GWTC-2.1	GW190521	$0.56^{+0.36}_{-0.27}$	$98.4^{+33.6}_{-21.7}$	$57.2^{+27.1}_{-30.1}$	$147.4^{+40.0}_{-16.0}$	$0.71^{+0.12}_{-0.16}$	19.51	BBH
GWTC-2.1	GW190521_074359	$0.21^{+0.10}_{-0.10}$	$43.4^{+5.8}_{-5.5}$	$33.4^{+5.2}_{-6.8}$	$72.6^{+6.5}_{-5.4}$	$0.72^{+0.05}_{-0.07}$	19.26	BBH
GWTC-2.1	GW190527_092055	$0.44^{+0.29}_{-0.19}$	$35.6^{+18.7}_{-8.0}$	$22.2^{+9.0}_{-8.7}$	$55.5^{+17.9}_{-8.5}$	$0.71^{+0.12}_{-0.16}$	18.91	BBH
GWTC-2.1	GW190620_030421	$0.50^{+0.23}_{-0.20}$	$58.0^{+19.2}_{-13.3}$	$35.0^{+13.1}_{-14.5}$	$88.0^{+17.2}_{-12.4}$	$0.79^{+0.08}_{-0.15}$	19.36	BBH
GWTC-2.1	GW190706_222641	$0.60^{+0.33}_{-0.29}$	$74.0^{+20.1}_{-16.9}$	$39.4^{+18.4}_{-15.4}$	$107.3^{+25.2}_{-15.9}$	$0.78^{+0.09}_{-0.18}$	19.90	BBH
GWTC-2.1	GW190719_215514	$0.61^{+0.39}_{-0.30}$	$36.6^{+42.1}_{-11.1}$	$19.9^{+10.0}_{-9.3}$	$54.5^{+38.3}_{-11.1}$	$0.78^{+0.11}_{-0.17}$	18.84	BBH
GWTC-2.1	GW190720_000836	$0.16^{+0.11}_{-0.05}$	$14.2^{+5.6}_{-3.3}$	$7.5^{+2.2}_{-1.8}$	$20.8^{+3.9}_{-2.0}$	$0.72^{+0.06}_{-0.05}$	17.94	BBH
GWTC-2.1	GW190727_060333	$0.52^{+0.18}_{-0.18}$	$38.9^{+8.9}_{-6.0}$	$30.2^{+6.5}_{-8.3}$	$65.4^{+9.5}_{-7.3}$	$0.73^{+0.10}_{-0.10}$	18.91	BBH
GWTC-2.1	GW190728_064510	$0.18^{+0.05}_{-0.07}$	$12.5^{+6.9}_{-2.3}$	$8.0^{+1.7}_{-2.6}$	$19.7^{+4.4}_{-1.4}$	$0.71^{+0.04}_{-0.04}$	17.79	BBH
GWTC-2.1	GW190828_063405	$0.38^{+0.10}_{-0.15}$	$31.9^{+5.4}_{-4.1}$	$25.8^{+4.9}_{-5.3}$	$54.3^{+7.3}_{-4.0}$	$0.75^{+0.06}_{-0.07}$	18.91	BBH
GWTC-2.1	GW190930_133541	$0.16^{+0.06}_{-0.06}$	$14.2^{+8.0}_{-4.0}$	$6.9^{+2.4}_{-2.1}$	$20.2^{+6.1}_{-2.0}$	$0.72^{+0.07}_{-0.06}$	17.79	BBH
GWTC-3	GW191103_012549	$0.20^{+0.09}_{-0.09}$	$11.8^{+6.2}_{-2.2}$	$7.9^{+1.7}_{-2.4}$	$19.0^{+3.8}_{-1.7}$	$0.75^{+0.06}_{-0.05}$	17.94	BBH
GWTC-3	GW191126_115259	$0.30^{+0.12}_{-0.13}$	$12.1^{+5.5}_{-2.2}$	$8.3^{+1.9}_{-2.4}$	$19.6^{+3.5}_{-2.0}$	$0.75^{+0.06}_{-0.05}$	17.94	BBH
GWTC-3	GW191127_050227	$0.57^{+0.40}_{-0.29}$	53^{+47}_{-20}	24^{+17}_{-14}	76^{+39}_{-21}	$0.75^{+0.13}_{-0.29}$	19.45	BBH
GWTC-3	GW191204_110529	$0.34^{+0.25}_{-0.18}$	$27.3^{+11.0}_{-6.0}$	$19.3^{+5.6}_{-6.0}$	$45.0^{+8.6}_{-7.6}$	$0.71^{+0.12}_{-0.11}$	18.54	BBH
GWTC-3	GW191204_171526	$0.13^{+0.04}_{-0.05}$	$11.9^{+3.3}_{-1.8}$	$8.2^{+1.4}_{-1.6}$	$19.21^{+1.79}_{-0.95}$	$0.73^{+0.03}_{-0.03}$	17.79	BBH
GWTC-3	GW200112_155838	$0.24^{+0.07}_{-0.08}$	$35.6^{+6.7}_{-4.5}$	$28.3^{+4.4}_{-5.9}$	$60.8^{+5.3}_{-4.3}$	$0.71^{+0.06}_{-0.06}$	18.76	BBH
GWTC-3	GW200128_022011	$0.56^{+0.28}_{-0.28}$	$42.2^{+11.6}_{-8.1}$	$32.6^{+9.5}_{-9.2}$	71^{+16}_{-11}	$0.74^{+0.10}_{-0.10}$	19.11	BBH
GWTC-3	GW200129_065458	$0.18^{+0.05}_{-0.07}$	$34.5^{+9.9}_{-3.2}$	$28.9^{+3.4}_{-9.3}$	$60.3^{+4.0}_{-3.3}$	$0.73^{+0.06}_{-0.05}$	18.99	BBH
GWTC-3	GW200208_222617	$0.66^{+0.53}_{-0.29}$	51^{+103}_{-30}	$12.3^{+9.2}_{-5.5}$	61^{+99}_{-26}	$0.83^{+0.14}_{-0.27}$	19.14	BBH
GWTC-3	GW200220_061928	$0.90^{+0.55}_{-0.40}$	87^{+40}_{-23}	61^{+26}_{-25}	141^{+51}_{-31}	$0.71^{+0.15}_{-0.17}$	19.36	BBH
GWTC-3	GW200224_222234	$0.32^{+0.08}_{-0.11}$	$40.0^{+6.9}_{-4.5}$	$32.5^{+5.0}_{-7.2}$	$68.6^{+6.6}_{-4.7}$	$0.73^{+0.07}_{-0.07}$	19.21	BBH
GWTC-3	GW200306_093714	$0.38^{+0.24}_{-0.18}$	$28.3^{+17.1}_{-7.7}$	$14.8^{+6.5}_{-6.4}$	$41.7^{+12.3}_{-6.9}$	$0.78^{+0.11}_{-0.26}$	18.61	BBH
GWTC-3	GW200308_173609	$1.04^{+1.47}_{-0.57}$	60^{+166}_{-29}	24^{+36}_{-13}	88^{+169}_{-47}	$0.91^{+0.03}_{-0.08}$	20.20	BBH
GWTC-3	GW200322_091133	$0.59^{+1.43}_{-0.32}$	50^{+132}_{-22}	$11.3^{+24.3}_{-6.0}$	48^{+132}_{-22}	$0.78^{+0.16}_{-0.17}$	18.91	BBH
GWTC-4.0	GW230814_230901	$0.06^{+0.03}_{-0.03}$	$33.6^{+2.8}_{-2.2}$	$28.3^{+2.1}_{-3.0}$	$58.9^{+1.9}_{-1.9}$	$0.71^{+0.04}_{-0.05}$	19.36	BBH
GWTC-4.0	GW231028_153006	$0.67^{+0.18}_{-0.27}$	$95.0^{+33.0}_{-20.0}$	$58.0^{+21.0}_{-25.0}$	$144.0^{+27.0}_{-13.0}$	$0.77^{+0.08}_{-0.08}$	19.60	BBH
GWTC-4.0	GW231226_101520	$0.23^{+0.04}_{-0.06}$	$40.1^{+4.4}_{-2.9}$	$35.0^{+3.2}_{-4.9}$	$71.4^{+3.8}_{-2.8}$	$0.73^{+0.05}_{-0.04}$	19.11	BBH

306018/2025-0), and FAPESP (grant No. 2021/01089-1).

[1] A. Aab *et al.* (Pierre Auger), Measurement of the cosmic-ray energy spectrum above 2.5×10^{18} eV using the Pierre Auger Observatory, Phys. Rev. D **102**, 062005 (2020), arXiv:2008.06486 [astro-ph.HE].

[2] T. Abu-Zayyad *et al.*, The Cosmic-Ray Energy Spectrum Observed with the Surface Detector of the Telescope Array Experiment, ApJL **768**, L1 (2013), arXiv:1205.5067 [astro-ph.HE].

[3] K. Kotera and A. V. Olinto, The Astrophysics of Ultrahigh-Energy Cosmic Rays, ARAA **49**, 119 (2011), arXiv:1101.4256 [astro-ph.HE].

[4] L. A. Anchordoqui, Ultra-high-energy cosmic rays, Physics Reports **801**, 1 (2019), arXiv:1807.09645 [astro-ph.HE].

[5] K. Greisen, End to the Cosmic-Ray Spectrum?, PRL **16**, 748 (1966).

[6] G. T. Zatsepin and V. A. Kuz'min, Upper Limit of the Spectrum of Cosmic Rays, Soviet Journal of Experimental and Theoretical Physics Letters **4**, 78 (1966).

[7] E. Mayotte, Measurement and Interpretation of UHECR Mass Composition at the Pierre Auger Observatory, arXiv e-prints , arXiv:2507.10292 (2025), arXiv:2507.10292 [astro-ph.HE].

[8] A. Halim *et al.* (Pierre Auger Collaboration), Inference of the Mass Composition of Cosmic Rays with Energies from 1018.5 to 1020 eV Using the Pierre Auger Observatory and Deep Learning, PRL **134**, 021001 (2025), arXiv:2406.06315 [astro-ph.HE].

[9] F. Fraschetti, On the acceleration of ultra-high-energy cosmic rays, Philosophical Transactions of the Royal Society of London Series A **366**, 4417 (2008), arXiv:0809.3057 [astro-ph].

[10] A. R. Bell, The acceleration of cosmic rays in shock fronts - I., MNRAS **182**, 147 (1978).

[11] A. R. Bell, Cosmic ray acceleration, Astroparticle Physics **43**, 56 (2013), arXiv:1301.7041 [astro-ph.HE].

[12] A. Spitkovsky, Particle acceleration in relativistic collisionless shocks: Fermi process at last?, Astrophys. J. Lett. **682**, L5 (2008), arXiv:0802.3216 [astro-ph].

[13] D. Caprioli and A. Spitkovsky, Simulations of ion acceleration at non-relativistic shocks. i. acceleration efficiency, Astrophys. J. **783**, 91 (2014), arXiv:1310.2943 [astro-ph.HE].

[14] N. W. Schween, F. Schulze, and B. Reville, Sapphire++: A particle transport code combining a spherical harmonic expansion and the discontinuous Galerkin method, Journal of Computational Physics **523**, 113690 (2025), arXiv:2501.05110 [astro-ph.HE].

[15] A. Shirin T, B. Reville, N. W. Schween, F. Schulze, and J. G. Kirk, Spectral curvature and breaks from Fermi acceleration at oblique shocks, MNRAS **544**, L160 (2025), arXiv:2511.01635 [astro-ph.HE].

[16] R. J. Protheroe and T. Stanev, Cut-offs and pile-ups in shock acceleration spectra, Astroparticle Physics **10**, 185 (1999), arXiv:astro-ph/9808129 [astro-ph].

[17] L. N. Padilha and R. C. Dos Anjos, Oblique Shocks at Supernova Remnants in Massive Star Clusters: A Model for the Cosmic-Ray Knee Observed by LHAASO, ApJ **1002**, 97 (2026), arXiv:2604.07977 [astro-ph.HE].

[18] C. H. Coimbra Araujo and R. C. Anjos, Rotating black holes with magnetic fields as accelerators of charged particles, in *International Conference on Black Holes as Cosmic Batteries: UHECRs and Multimessenger Astronomy. 12-15 September 2018. Foz do Iguaçu* (2018) p. 5.

[19] C. H. Coimbra-Araújo and R. C. Anjos, Acceleration of charged particles from near-extremal rotating black holes embedded in magnetic fields, Classical and Quantum Gravity **38**, 015007 (2021), arXiv:2005.13599 [gr-qc].

[20] C. H. Coimbra-Araújo and R. C. dos Anjos, Ultra-High-Energy Particles at the Border of Kerr Black Holes Triggered by Magnetocentrifugal Winds, Galaxies **10**, 84 (2022).

[21] M. Bañados, J. Silk, and S. M. West, Kerr Black Holes as Particle Accelerators to Arbitrarily High Energy, PRL **103**, 111102 (2009), arXiv:0909.0169 [hep-ph].

[22] J. M. Bardeen, W. H. Press, and S. A. Teukolsky, Rotating Black Holes: Locally Nonrotating Frames, Energy Extraction, and Scalar Synchrotron Radiation, ApJ **178**, 347 (1972).

[23] T. Jacobson and T. P. Sotiriou, Spinning Black Holes as Particle Accelerators, PRL **104**, 021101 (2010), arXiv:0911.3363 [gr-qc].

[24] S.-W. Wei, Y.-X. Liu, H. Guo, and C.-E. Fu, Charged spinning black holes as particle accelerators, PRD **82**, 103005 (2010), arXiv:1006.1056 [hep-th].

[25] V. P. Frolov, Weakly magnetized black holes as particle accelerators, PRD **85**, 024020 (2012), arXiv:1110.6274 [gr-qc].

[26] T. Igata, T. Harada, and M. Kimura, Effect of a weak electromagnetic field on particle acceleration by a rotating black hole, PRD **85**, 104028 (2012), arXiv:1202.4859 [gr-qc].

[27] M. Bejger, T. Piran, M. Abramowicz, and F. Håkanson, Collisional Penrose Process near the Horizon of Extreme Kerr Black Holes, PRL **109**, 121101 (2012), arXiv:1205.4350 [astro-ph.HE].

[28] O. B. Zaslavskii, Energetics of particle collisions near dirty rotating extremal black holes: Banados-Silk-West effect versus Penrose process, PRD **86**, 084030 (2012), arXiv:1205.4410 [gr-qc].

[29] T. Harada, H. Nemoto, and U. Miyamoto, Upper limits of particle emission from high-energy collision and reaction near a maximally rotating kerr black hole, Phys. Rev. D **86**, 024027 (2012).

[30] J. D. Schnittman, Revised Upper Limit to Energy Extraction from a Kerr Black Hole, PRL **113**, 261102 (2014), arXiv:1410.6446 [astro-ph.HE].

[31] O. B. Zaslavskii, Unbounded energies of debris from head-on particle collisions near black holes, Modern Physics Letters A **30**, 1550076 (2015), arXiv:1411.0267 [gr-qc].

[32] E. Berti, R. Brito, and V. Cardoso, Ultrahigh-Energy Debris from the Collisional Penrose Process, PRL **114**, 251103 (2015), arXiv:1410.8534 [gr-qc].

[33] O. B. Zaslavskii, Ultrahigh energy particle collisions near the black hole horizon in the strong magnetic field, Modern Physics Letters A **29**, 1450112 (2014), arXiv:1403.6286 [gr-qc].

[34] D. Ehlert, F. Oikonomou, and E. Peretti, Ultra-high-energy cosmic rays from ultra-fast outflows of active galactic nuclei, MNRAS **539**, 2435 (2025), arXiv:2411.05667 [astro-ph.HE].

[35] G. R. Farrar, Binary Neutron Star Mergers as the Source of the Highest Energy Cosmic Rays, PRL **134**, 081003 (2025), arXiv:2405.12004 [astro-ph.HE].

[36] G. R. Farrar, Ultra-High-energy Cosmic Ray Production in Binary Neutron Star Mergers, ApJL **994**, L7 (2025), arXiv:2506.22625 [astro-ph.HE].

[37] J. P. Pereira, C. H. Coimbra-Araújo, R. C. dos Anjos, and J. G. Coelho, Binary Coalescences as Sources of Ultrahigh-Energy Cosmic Rays, PRL **132**, 091401 (2024), arXiv:2307.06200 [astro-ph.HE].

[38] R. Abbott *et al.* (LIGO Scientific Collaboration and Virgo Collaboration), GWTC-2: Compact Binary Coalescences Observed by LIGO and Virgo during the First Half of the Third Observing Run, Phys. Rev. X **11**, 021053 (2021), arXiv:2010.14527 [gr-qc].

[39] R. Abbott *et al.* (LIGO Scientific Collaboration and Virgo Collaboration), GWTC-3: Compact Binary Coalescences Observed by LIGO and Virgo during the Second Part of the Third Observing Run, Phys. Rev. X **13**, 041039 (2023), arXiv:2111.03606 [gr-qc].

[40] R. Abbott *et al.* (LIGO Scientific Collaboration, Virgo Collaboration, and KAGRA Collaboration), Population of Merging Compact Binaries Inferred Using Gravitational Waves through GWTC-3, Phys. Rev. X **13**, 011048 (2023), arXiv:2111.03634 [astro-ph.HE].

[41] M. Zilhão, V. Cardoso, C. Herdeiro, L. Lehner, and U. Sperhake, Collisions of charged black holes, PRD **85**, 124062 (2012), arXiv:1205.1063 [gr-qc].

[42] M. Obergaulinger, M. A. Aloy, and E. Müller, Local simulations of the magnetized Kelvin-Helmholtz instability in neutron-star mergers, A&A **515**, A30 (2010), arXiv:1003.6031 [astro-ph.SR].

[43] B. Giacomazzo, J. Zrake, P. C. Duffell, A. I. MacFadyen, and R. Perna, Producing Magnetar Magnetic Fields in the Merger of Binary Neutron Stars, ApJ **809**, 39 (2015), arXiv:1410.0013 [astro-ph.HE].

[44] K. Kiuchi, Y. Sekiguchi, K. Kyutoku, M. Shibata, K. Taniguchi, and T. Wada, High resolution magnetohydrodynamic simulation of black hole-neutron star merger: Mass ejection and short gamma ray bursts, PRD **92**, 064034 (2015), arXiv:1506.06811 [astro-ph.HE].

[45] M. Ruiz, R. N. Lang, V. Paschalidis, and S. L. Shapiro, Binary Neutron Star Mergers: A Jet Engine for Short Gamma-Ray Bursts, ApJL **824**, L6 (2016), arXiv:1604.02455 [astro-ph.HE].

[46] C. Palenzuela, R. Aguilera-Miret, F. Carrasco, R. Ciolfi, J. V. Kalinani, W. Kastaun, B. Miñano, and D. Viganò, Turbulent magnetic field amplification in binary neutron star mergers, Phys. Rev. D **106**, 023013 (2022).

[47] D. Radice, S. Bernuzzi, and A. Perego, The Dynamics of Binary Neutron Star Mergers and GW170817, Annual Review of Nuclear and Particle Science **70**, 95 (2020), arXiv:2002.03863 [astro-ph.HE].

[48] R. Aguilera-Miret, J.-E. Christian, S. Rosswog, and C. Palenzuela, Robustness of Magnetic Field Amplification in Neutron Star Mergers, MNRAS **542**, 3067 (2025), arXiv:2504.10604 [astro-ph.HE].

[49] R. Ciolfi, The key role of magnetic fields in binary neutron star mergers, General Relativity and Gravitation **52**, 59 (2020), arXiv:2003.07572 [astro-ph.HE].

[50] B. Margalit and B. D. Metzger, Constraining the Maximum Mass of Neutron Stars from Multi-messenger Observations of GW170817, ApJL **850**, L19 (2017).

[51] M. Shibata and K. Hotokezaka, Merger and Mass Ejection of Neutron-Star Binaries, Annual Review of Nuclear and Particle Science **69**, 41 (2019).

[52] V. P. Frolov, Weakly magnetized black holes as particle accelerators, PRD **85**, 024020 (2012).

[53] O. B. Zaslavskii, Acceleration of particles by black holes: General considerations, PRD **82**, 083004 (2010).

[54] K. Kiuchi, K. Kyutoku, Y. Sekiguchi, and M. Shibata, Global simulations of strongly magnetized remnant massive neutron stars formed in binary neutron star mergers, Phys. Rev. D **97**, 124039 (2018).

[55] F. Foucart, A. Chernoglazov, M. Boyle, T. Hinderer, M. Miller, J. Moxon, M. A. Scheel, N. Deppe, M. D. Duez, F. Hébert, L. E. Kidder, W. Throwe, and H. P. Pfeiffer, High-accuracy waveforms for black hole-neutron star systems with spinning black holes, PRD **103**, 064007 (2021), arXiv:2010.14518 [gr-qc].

[56] H. Falcke and L. Rezzolla, Fast radio bursts: the last crack of doom, A&A **562**, A137 (2014).

[57] B. P. Abbott *et al.*, Multi-messenger Observations of a Binary Neutron Star Merger, ApJL **848**, L12 (2017).

[58] E. W. Leaver, An analytic representation for the quasinormal modes of kerr black holes, Proceedings of the Royal Society of London. A. Mathematical and Physical Sciences **402**, 285 (1985).

[59] E. Berti, V. Cardoso, and A. O. Starinets, Quasinormal modes of black holes and black branes, Classical and Quantum Gravity **26**, 163001 (2009), arXiv:0905.2975 [gr-qc].

[60] D. Reitze, R. X. Adhikari, S. Ballmer, B. Barish, L. Barsotti, G. Billingsley, D. A. Brown, Y. Chen, D. Coyne, R. Eisenstein, M. Evans, P. Fritschel, E. D. Hall, A. Lazzarini, G. Lovelace, J. Read, B. S. Sathyaprakash, D. Shoemaker, J. Smith, C. Torrie, S. Vitale, R. Weiss, C. Wipf, and M. Zucker, Cosmic Explorer: The U.S. Contribution to Gravitational-Wave Astronomy beyond LIGO, in *Bulletin of the American Astronomical Society*, Vol. 51 (2019) p. 35, arXiv:1907.04833 [astro-ph.IM].

[61] M. Maggiore, C. Van Den Broeck, N. Bartolo, E. Belgacem, D. Bertacca, M. A. Bizouard, M. Branchesi, S. Clesse, S. Foffa, J. García-Bellido, S. Grimm, J. Harms, T. Hinderer, S. Matarrese, C. Palomba, M. Peloso, A. Ricciardone, and M. Sakellariadou, Science case for the Einstein telescope, JCAP **2020**, 050 (2020), arXiv:1912.02622 [astro-ph.CO].

[62] G. A. Anastasi and Pierre Auger Collaboration, Auger-Prime: The Pierre Auger Observatory upgrade, Nuclear Instruments and Methods in Physics Research A **1044**, 167497 (2022).

[63] A. V. Olinto, J. Krizmanic, J. H. Adams, R. Aloisio, L. A. Anchordoqui, A. Anzalone, M. Bagheri, D. Barghini, M. Battisti, D. R. Bergman, *et al.*, The poemma (probe of extreme multi-messenger astrophysics) observatory, J. Cosmology Astropart. Phys. **2021**, 007 (2021), arXiv:2012.07945 [astro-ph.HE].

[64] GRAND Collaboration, J. Alvarez-Muñiz, R. Alves Batista, A. Balagopal V., J. Bončius, M. Bustamante, W. Carvalho, D. Charrier, I. Cognard, V. Decoene, *et al.*, The giant radio array for neutrino detection (grand): Science and design, Science China Physics, Mechanics, and Astronomy **63**, 219501 (2020), arXiv:1810.09994 [astro-ph.HE].

[65] S. C. de Léon *et al.* (CREDO Collaboration), Cosmic-ray extremely distributed observatory, Symmetry **12**, 1835 (2020).